Journal of Colloid and Interface Science 592 (2021) 195–204

Contents lists available at ScienceDirect

Journal of Colloid and Interface Science

journal homepage: www.elsevier.com/locate/jcis

Regular Article

Modelling and simulation of field directed linear assembly of aerosol particles

Prithwish Biswas [a], Pankaj Ghildiyal [a,b], George W. Mulholland [b], Michael R. Zachariah [a,*]

[a] University of California, Riverside, CA 92521, United States
[b] University of Maryland, College Park, MD 20742, United States

GRAPHICAL ABSTRACT

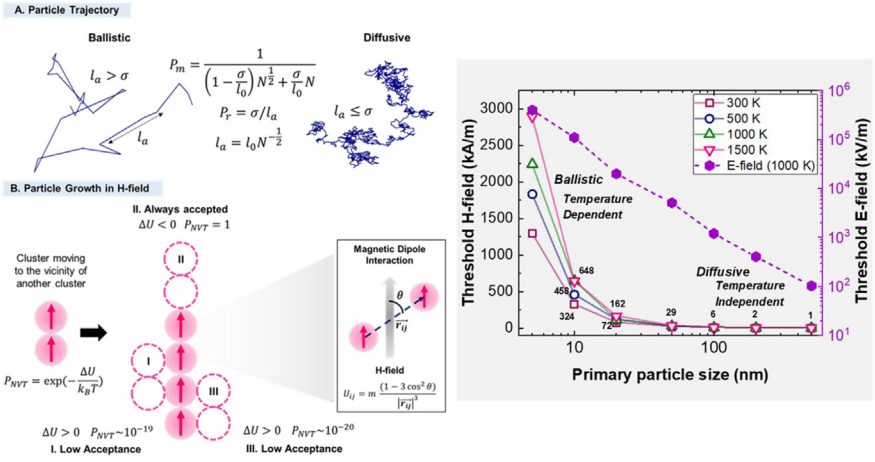

ARTICLE INFO

Article history:
Received 1 December 2020
Revised 19 January 2021
Accepted 11 February 2021
Available online 19 February 2021

Keywords:
Aerosol particle assembly
Field directed assembly
Linear chain aggregates
Coagulation kernel
Free molecular regime

ABSTRACT

Unlike liquid phase colloidal assembly, significantly changing the structure of fractal aggregates in the aerosol phase, is considered impractical. In this study, we discuss the possibility of applying external magnetic and electric fields, to tune the structure and fractal dimension (D_f) of aggregates grown in the aerosol phase. We show that external fields can be used to induce dipole moments in primary nanoparticles. We found that an ensemble of particles with induced dipole moments will interact through directional attractive and repulsive forces, leading to the formation of linear, chain-like aggregates with $D_f \sim 1$. The aggregate structure transition is dependent on the primary particle sizes, temperature and applied field strength which was evaluated by performing a hybrid ensemble/cluster-cluster aggregation Monte Carlo simulation. We demonstrate that the threshold magnetic field strength required to linearly assemble 10–500 nm particle sizes are practically achievable whereas the electric field required to assemble sub-100 nm particles are beyond the breakdown strength of most gases. To theoretically account for the enhanced coagulation rates due to attractive interactions, we have also derived a correction factor to both free molecular and transition regime coagulation kernel, based on magnetic dipolar interactions. A comparison has been made between the coagulation time-scales estimated by theory and simulation, with the estimated magnetization time-scales of the primary particles along with oscillation time period of the magnetic field, to demonstrate that sub-50 nm superparamagnetic primary

* Corresponding author.
E-mail address: mrz@engr.ucr.edu (M.R. Zachariah).

https://doi.org/10.1016/j.jcis.2021.02.050

particles can be magnetized and assembled at any temperature, while below the Curie temperature ferromagnetic particles of all sizes can be magnetized and assembled, given the applied field is higher than the threshold.

List of frequently used abbreviations and symbols

k_B	Boltzmann Constant	N	Number of monomers in aggregate
T	Temperature	m_g	Mass of medium gas molecule
$\langle x^2(t)\rangle$	Mean-squared displacement	p	Dipole moment
ξ	Drag coefficient	r_{ij}	Pairwise interparticle radial distance
l_a	Persistence length (Aggregate)	U_{ij}	Pairwise interparticle interaction potential
l_0	Persistence length (monomer)	α	Polarizability
m_p	Mass (monomer)	μ_r	Relative permeability
r_p	Radius (monomer)	μ_0	Free-space permeability
H	Magnetic field strength	θ	Angle between radial vector and field
τ_s	Néel relaxation time	τ_B	Brownian rotational time
σ	Monomer diameter/unit of length	$t_{1/2}$	Half-life
D_f	Fractal dimension	$g(r/\sigma)$	Pair-correlation function

1. Introduction

Aerosol routes comprise one of the primary approaches to submicron particle production at the industrial scale [1]. However, considerable research has been expended in modification to common aerosol routes, such as laser ablation [2], sputtering [3], vapor phase decomposition [1] in an a effort to better control and affect chemistry, crystallinity and size distribution [4–7]. However, most of these commonly used aerosol routes result in considerable aggregation at practical particle densities, leading to close compact aggregates, resulting from rapid Brownian motion [8].

During the formation of sub-micron particles by nucleation, the aerosol typically transitions from free-molecule transport to the continuum. This is in contrast with liquid-phase synthesis techniques which are always in the continuum regime, and Brownian dynamics are orders of magnitude slower. Furthermore, in the liquid phase surface charges or polymer coatings are often employed to manipulate colloidal stability to enable manipulation of particle assembly [9]. In contrast and unfortunately, irreversible sticking of particles in the aerosol phase, due to short range inter-particle attractive forces (commonly represented by hard-sphere Hamaker forces) [10], offer little ability to slow down coagulation. The resulting coagulation in the gas phase leads to a self-similar aggregate structure, which is commonly quantified by the universal fractal dimension (D_f) of ~1.8 [11]. To manipulate or otherwise slow coagulation, researchers have explored repulsive interactions such as unipolar charging, however this is quite challenging as uniform charging is typically inefficient, and very size dependent [12–14].

Relatively little work has been done to manipulate the fractal character of aggregates. In liquids dipolar interactions between particles can induce directional control of attractive and repulsive forces, which has been shown to form linear low-dimensional aggregates [15]. Through both experiments and simulations, it has been shown that liquid phase particles can be assembled into linear chains through induction of electric and magnetic dipolar interactions [15–18]. Apart from conservation of surface area, the linear assembly of particles have several applications in materials processing and design for mechanical and electromagnetic applications [19–21]. To our knowledge no previous experimental attempts have been made to assemble nanoparticles in aerosol phase which are in the free molecular regime. Also, the possibility of such an assembly in the aerosol phase have not been justified through theory or simulation before. Recently, our group has been able to synthesize nanoparticles (~10–20 nm) of ferromagnetic materials, Fe and Ni, from an electromagnetically levitated metal droplet and found that the magnetic field used for levitation, can be also be used to assemble any ferromagnetic particles into linear aggregates [22].

In this study we have combined the theories on Langevin dynamics of aerosol particles with the thermodynamics of ensemble of interacting particles, to perform a hybrid ensemble/cluster-cluster aggregation Monte Carlo simulation, of the aggregation and assembly of ferromagnetic particles in an applied magnetic field. We have considered different primary particle sizes in the range 5–500 nm, at various temperatures 300–1500 K, which cover both free molecular and transition regimes. We have shown that if the magnetic field is higher than a critical threshold, aggregate structure transitions from $D_f \sim 1.8$ to $D_f \sim 1$. As the assembly is heavily dependent on the particle size and temperature, the range of size and temperature for successful assembly have been evaluated along with the threshold magnetic field. Doing similar simulations with electric dipoles in electric field, a comparison has been drawn between the practical achievability of the threshold fields required in both cases. Time scales of magnetization of the primary particles of different sizes have been estimated to determine the sizes for which the induced magnetic dipolar alignment will be in equilibrium with the applied field, a condition which will ensure uniform interactions, and hence tunable assembly.

2. Theory, model and simulation procedure

2.1. Langevin equation in an ensemble of magnetic dipoles

The Langevin equation of motion has been shown to accurately explain the dynamics of small aerosol particles and aggregates in both ballistic and diffusive time scales in the free molecular and transition regime [23,24]. Several studies have also employed this equation to develop collision kernel by simulation of coagulation [25–29] and charging processes [12–14,26,30,31] of fractal aggregates in the aerosol phase which have also been experimentally validated [32,33]. The situation of interest to us, the presence

of an external magnetic field (H-field), ferromagnetic particles and aggregates have a net magnetic anisotropy along the direction of the magnetic field. As a result of the field induced anisotropy, the particle and particle aggregates behave as magnetic dipoles, and interact with each other through dipole-dipole interactions. The Langevin equation of 1-D motion of particles and aggregates moving in an ensemble with other similar entities can be represented by:

$$m\frac{d^2x}{dt^2} = -\xi\frac{dx}{dt} + F(t) + F_H \tag{1}$$

where m is the mass of the entity, ξ is the drag co-efficient, $F(t)$ is the random Brownian force acting on the entity which satisfies $\langle F(t)\rangle = 0$ and $\langle F(t)F(t')\rangle = 2\xi k_B T\delta(t-t')$ [34]. F_H, which is not present in the original Langevin equation for non-interacting particles, is the force on the entity due to dipolar interactions with other entities in the ensemble. As the dipolar interactions are short-ranged compared to the mean-displacement of the particles, F_H insignificantly affects the overall kinetics of the ensemble and can be ignored. However, it has a significant effect on the stability and structure of the aggregates. Hence, we have derived the expressions of the kinetic variables in the simulation solely based on the Brownian dynamics, by dropping the F_H term and only considering$F(t)$. The thermodynamics of the magnetic interactions have been dealt with by assuming the particles to be in a canonical (constant temperature) ensemble, which implies the average kinetic energy of the overall ensemble is conserved. After neglecting F_H, and by multiplying x on both sides of Eq. (1), doing a derivative transformation, applying the equipartition theorem ($m\langle v^2\rangle = k_B T$) and taking ensemble averages of the variables, (Section S.1, supplemental) we arrive at the time dependent solution of the mean square displacement, $\langle x^2(t)\rangle$ as given by Eq. (2) [35],

$$\langle x^2(t)\rangle = \frac{2k_BT}{\xi}\left(t - \frac{m}{\xi} + \frac{m}{\xi}e^{-\frac{\xi t}{m}}\right) \tag{2}$$

For the ballistic limit, $t \ll \frac{m}{\xi}$, we can approximate the exponential term in Eq. (2) by a third order series expansion, so that $\langle x^2(t)\rangle$ is given by $\langle x^2(t)\rangle = \frac{k_BT}{m}t^2$, which implies that the 3-D root-mean-squared displacement over the characteristic time scale $\frac{m}{\xi}$, also known as the persistence length (l_a) will be given, by:

$$l_a = \frac{\sqrt{3k_BTm}}{\xi} \tag{3}$$

In the free molecular regime ξ is given by [23]:

$$\xi = 4\pi\delta P\sqrt{\frac{m_g}{3k_bT}}r_p^2 N \tag{4}$$

where m_g is the mass of the ambient gas molecule, P is the ambient pressure (1 atm), δ is the accommodation coefficient (1.44 assuming N_2) [36], r_p is the radius of the primary particle, and N is the number of primary particles in the aggregate. In Eq. (3) m scales with the mobility radius (R_m) of the aggregate. It is known that R_m of aggregates formed by cluster-cluster aggregates scales with N as, $R_m\ N^{\frac{1}{2}}$ [37], and the aggregate mass, $m = m_pN$, m_p being the mass of

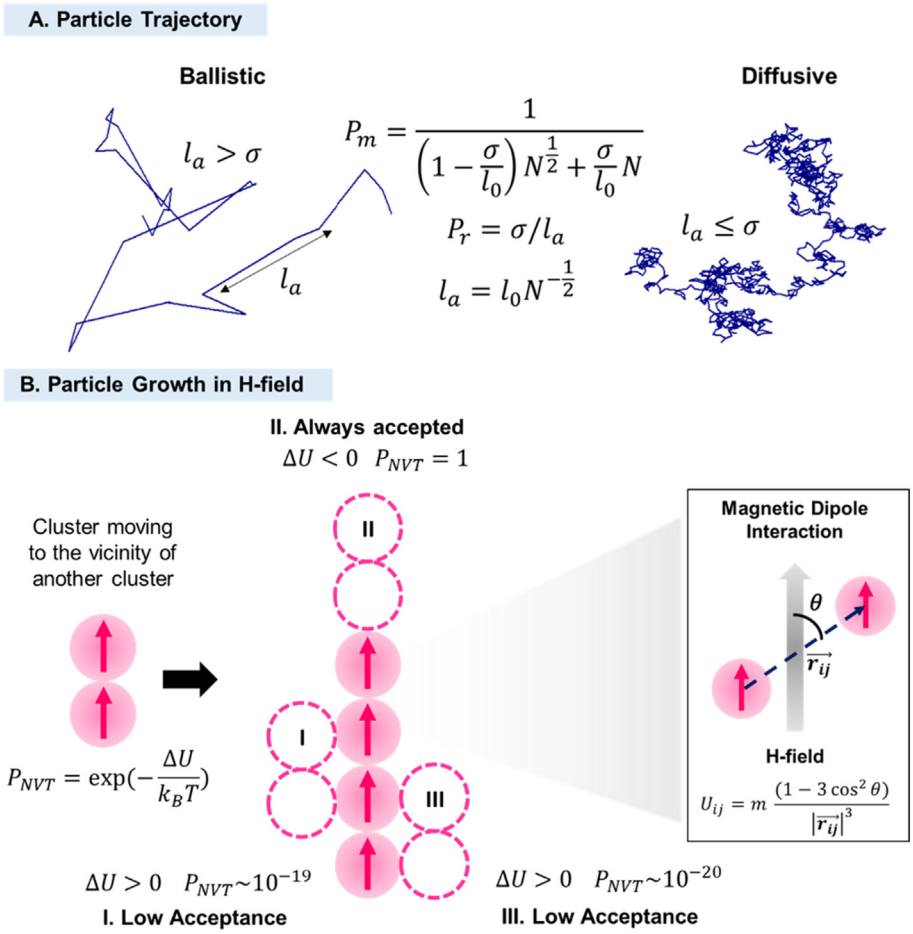

Fig. 1. Graphical representation of the simulation method, the movement trajectories (A), aggregate growth (B) and the magnetic dipolar interactions.

primary particle in the aggregate. Substituting for m and ξ from Eq. (4) into Eq. (3), the persistence length is given given by:

$$l_a = \frac{3k_BT}{4\pi\delta P}\sqrt{\frac{m_p}{m_g}}r_p^{-2}N^{-\frac{1}{2}} \tag{5}$$

The special case of $N = 1$, is the persistence length of a monomer (l_0) [23]. Physically, the persistence length signifies the length scale of ballistic linear motion of the primary particles or aggregates, as depicted in the schematic in Fig. 1. For small nanoparticles ~10 nm, in the free molecular regime, ballistic motion dominates the trajectory, and the persistence length is several times the diameter which implies that the particles will move several diameters without changing direction as shown by a representative trajectory in Fig. 1. In the diffusive limit, $t \gg \frac{m}{\xi}$ the 3-D mean squared displacement is equal to $\frac{6k_BT}{\xi}$, as given by the Einstein model [35]. For the diffusive limit, the persistence length is smaller, or on the order of the particle diameter, and the particle changes direction randomly, also shown in Fig. 1. For simulating aggregation of small particles in aerosol phase at high temperatures, accurately mimicking the ballistic limit is crucial.

2.2. Pairwise dipolar interaction potential in H-field

The potential energy (U_{ij}) of pairwise interaction between two spherical particles with magnetic dipoles with dipole moments $\vec{\boldsymbol{p}}_i$and $\vec{\boldsymbol{p}}_j$is given by [16]:

$$U_{ij} = \frac{1}{4\pi\mu_0\left|\vec{\boldsymbol{r}}_{\boldsymbol{ij}}\right|^3}\left[\vec{\boldsymbol{p}}_i.\vec{\boldsymbol{p}}_j - \frac{3\left(\vec{\boldsymbol{p}}_i.\vec{\boldsymbol{r}}_{\boldsymbol{ij}}\right)\left(\vec{\boldsymbol{p}}_j.\vec{\boldsymbol{r}}_{\boldsymbol{ij}}\right)}{\left|\vec{\boldsymbol{r}}_{\boldsymbol{ij}}\right|^2}\right] \tag{6}$$

When the magnitude of both dipoles are equivalent and aligned in the same direction as H-field, U_{ij} can be represented in scalar form as:

$$U_{ij} = \frac{p^2(1-3\cos^2\theta)}{4\pi\mu_0\left|\vec{\boldsymbol{r}}_{\boldsymbol{ij}}\right|^3} \tag{7}$$

where μ_0 is the permeability of free space, p is the magnitude of the dipoles,θ is the angle between $\vec{\boldsymbol{r}}_{\boldsymbol{ij}}$ and the H-field, a graphical representation of which has been shown in the schematic in Fig. 1. Both Eqs. (6) and (7), are for the $\left|\vec{\boldsymbol{r}}_{\boldsymbol{ij}}\right| \geq \boldsymbol{\sigma}$. The magnitude of the dipole moment is related to both material properties, and the strength of H-field, by $p = \alpha\sigma^3H$, where σ is the spherical particle diameter, H is the strength of the applied magnetic field, and α is the polarizability. The polarizability is related to the relative permeability (μ_r) of the material by:

$$\alpha = 4\pi\mu_0\left(\frac{\mu_r - 1}{\mu_r + 2}\right) \tag{8}$$

For ferromagnetic materials (Fe, Co, Ni etc.) in presence of an applied magnetic field, μ_r is large and ranges between ~10^2–10^3 [38–40]. Hence for ferromagnetic materials since $\mu_r \gg 1$, $\left(\frac{\mu_r-1}{\mu_r+2}\right) \to 1$, makes α $4\pi\mu_0$ a constant for all ferromagnetic materials. For paramagnetic materials, $\mu_r = 1$, which makes $\alpha = 0$, and hence there is no magnetic dipolar interactions. Since, α is a constant for ferromagnetic materials, the dipole moment is only a function of σ and H. To non-dimensionalize the interaction potential for simulation purposes, σ is used as the unit of length and k_BT_0 (T_0 = 300 K) as the unit of energy. In non-dimensionalized form, Eq. (7) will become $U_{ij} = \frac{q(1-3\cos^2\theta)}{r_{ij}^3}$, where r_{ij} is the non-dimensionalized radial distance between two particles and $q = \frac{p^2}{4\pi\mu_0\sigma^3k_BT_0}$ having dimension of energy. This implies the pairwise interaction energy which depends on $q\ \sigma^3H^2$, can be tuned by both particle size and strength of the magnetic field.

2.3. Hybrid canonical Ensemble/Cluster-Cluster aggregation Monte Carlo simulation of magnetic dipoles

The off-lattice MC simulation is performed with an initial configuration of 1000 primary particles of size σ placed in a cubic box of size $L = 60\sigma$. The simulations initiate with the motion of primary particles in an ensemble. After the appearance of the clusters due to collision and aggregation of the primary particles, movement of the clusters are also included for the remainder of the simulation. At every Monte Carlo step, a particle or an aggregate is chosen at random from the ensemble, and a decision is made on whether the chosen entity will be moved based on its mobility, imposing the diffusion limitation. The acceptance probability (P_m) of this decision depends inversely with the mobility radius (i.e. smaller aggregates are more likely to move) which is a function of number of primary particles in the aggregate (N) as given by:

$$P_m = \frac{1}{\left(1-\frac{\sigma}{l_0}\right)N^{\frac{1}{2}} + \frac{\sigma}{l_0}N} \tag{9}$$

The first term in the denominator represents the pure ballistic case when $\sigma \ll l_0$, whereas the second term represents the pure diffusive case when $\sigma = l_0$. The ballistic and diffusive regimes in the trajectory of the moving particle or aggregate is replicated by the fact that the chosen entity will move linearly over a distance of l_a before randomly changing direction under the influence of background gas. This is ensured by making a decision whether the particle or aggregate will keep moving in the same direction or assigned a new direction, determined by the probability P_r:,

$$P_r = \sigma/l_a \tag{10}$$

The center of mass of the selected aggregate is displaced by σ in the chosen direction. The move is then accepted or rejected based on an energy test, which compares the total energy due to magnetic interactions in the microstates before and after the move. The system follows the thermodynamics of canonical (NVT) ensemble. Hence, the acceptance probability (P_{NVT}) is:[41,42]

$$P_{NVT} = \exp\left(-\frac{\Delta U}{k_BT}\right) \tag{11}$$

where $\Delta U = \sum_{final}U_{ij} - \sum_{initial}U_{ij}$, is the difference in net pairwise interaction potentials in the initial and the final states. Once the decision is made to accept the move, the non-dimensionalized time is incremented by $1/N_t$, where N_t is the total number of entities in the ensemble including both aggregates and isolated primary particles (monomers). The unit of time is given by the characteristic time-scale of m/ξ normalized by the persistence length. When two lone primary particles or primary particles belonging to two different aggregates moves within a center to center distance of $< 1.1\sigma$, they are assumed to have collided and stuck irreversibly. The simulation is run till the number concentration of the monomers decreases to <10% of the initial value. Periodic boundary conditions with minimum image convention has been considered throughout the simulation.

2.4. Stability analysis of magnetic dipolar aggregates

The aggregation time-scales are estimated by the homogeneous monomer collision approximation of the Smoluchowski's equation, which is given by $n_1(t) = \frac{n_0}{1+n_0Kt}$ where $n_1(t)$ is the number concentration of monomers at time t, n_0 is the initial number

concentration of monomers and $K(1,1)$ is the monomer collision kernel [36]. In the continuum regime, K is related to the medium viscosity (η), ~1.8 × 10^{-5} Pa-s for N_2, and temperature (T) as $K = 8k_BT/3\eta$ [8]. In free molecular regime, K is related to particle diameter (σ), density (ρ) and T by $K = 4\left(\frac{6\sigma k_BT}{\rho}\right)^{1/2}$ [43].

However, the attractive particle interaction introduced by the H-field enhances K, increasing the coagulation rate. Hence, a correction factor (W) have been derived (Section S.2, supplemental) for both free molecular (W_{FM}) [31] and continuum (W_C) [8,44] regimes to estimate the coagulation kernel in the magnetic field (K_m), $K_m = KW$. The non-dimensionalized expressions of W_{FM} and W_C are given by:

$$W_{FM} = 2\int_0^\infty e^{-v^2} v^3 \left(1 + \frac{q}{2T' v^2}\right) dv$$

$$W_C = \frac{1}{\int_1^\infty \frac{\exp\left(-\frac{q}{2r_{ij}^3 T'}\right)}{r_{ij}^2} dr_{ij}} \tag{12}$$

where $T' = k_BT/k_BT_0$ is the non-dimensionalized parameter for thermal energy, v is the non-dimensionalized velocity, $q = \frac{p^2}{4\pi\mu_0\sigma^3 k_BT_0}$, as shown in Section 2.2 is a non-dimensional measure of the magnetic interaction energy. The non-dimensionalized form of the transition regime K derived by more recent mean first passage time regression studies [25,31], is a function of the diffusive Knudsen number (Kn_D). Accounting for the magnetic field enhancement correction inKn_D, $Kn_D = \frac{\sqrt{2k_BTm_p}W_C}{6\pi\eta\sigma^2 W_{FM}}$, the enhanced transition regime kernel can be estimated [31] (Section S.2, supplemental). The corrected kernel, K_m has been used to estimate the half-life of the monomer concentration, to draw comparison between the theoretical and simulated coagulation time-scales, which is compared with the magnetic domain relaxation and H-field oscillation time-scales to determine the conditions for which the simulation is applicable. All theoretical estimations have been done using material properties of Fe for the particle and N_2 for the medium.

3. Results and discussions

3.1. Aggregate shape transition with H field

The aggregation of non-interacting or weakly-interacting nanoparticles in the aerosol phase formed by diffusion limited cluster aggregation (DLCA), leads to the formation of aggregates of universal fractal dimension, D_f ~ 1.8. However, the presence of sufficiently strong inter-particle interactions can change the aggregation rate and assembly process leading to an altered fractal dimension. In our case we are applying a strong external magnetic field. Fig. 2(a) shows visual representations of aggregates formed by primary particles of size $\sigma = 10nm$ at $T = 1500$ K, in absence and presence of H-field. In absence of an external H-field typical DLCA aggregate of D_f ~ 1.7 is obtained. In the presence of H-field of strength 450 kA/m, induced magnetic dipole moments of the primary particles, influence the aggregation process, and low dimensional (D_f ~ 1.5) aggregates are obtained. When stronger H-fields (650 kA/m) are applied, the increased induced dipole strength leads to the formation of linear, chain-like 1-D aggregates.

Fig. 2(b) shows the intra-cluster pair correlation function $g(r/\sigma)$ averaged over all the aggregates formed in the ensemble in presence and absence of the H-field. The D_f is estimated from the scaling law of $g\left(\frac{r}{\sigma}\right) \left(\frac{r}{\sigma}\right)^{3-D_f}$. The typical feature of the pair correlation function of DLCA aggregates in a log-scale consists of the highest peak at $r = \sigma$ due to occupied nearest neighbor sites, followed by a peak at $r = 2\sigma$, as only those second nearest neighbor sites are occupied which lie along the same linear direction as that of the first occupied nearest neighbor. This feature suggests a shape that has lower dimensionality than 2. A linearly decreasing trend follows the second peak and is used to estimate the D_f. The linear trend is terminated by a sharply decreasing cut-off region which follows the trend $\exp(-\frac{r}{R_g}^{\gamma})$, $R_g$being the radius of gyration andγ ~2–2.5 (supplemental Fig. S2), as also observed by several studies[37,45,46]. In Fig. 2(b), the pair-correlation function of the aggregates formed in absence of the H-field has all the features as that of typical DLCA, with the estimated D_f 1.7. In the presence of 450 kA/m H-field the slope of the linear scaling region increases due to a smaller D_f ~ 1.5, whereas in presence of stronger 650 kA/m H-field, the pair-correlation function has some additional peaks and valleys features, with an estimated D_f 1. The peaks and valleys are at integral multiples of particle diameter (σ), and signifies that all the occupied neighboring sites lie along the same linear direction which in-turn signifies the formation of linear chain-like 1D structures. The peak values of straight linear chains of spheres exactly follows the power law, and the cut-off region arising due to dissimilar lengths follows the trend $e^{-r^{\gamma}}$ (supplemental, Fig. S3 and S4).

The fact that the linear structures are also aligned along the direction of H-field suggests that aggregate growth has been favored only in a unique direction, as the attractive potential is strongest at the terminal edges of the aggregates whereas the repulsive potential is strongest at the lateral edges. Hence, from both the visual representation, and the pair-correlation function it can be said that both the dimensionality and the directionality of growth of ferromagnetic particles can be tuned by applying an external H-field. However, significant high magnitude of magnetic

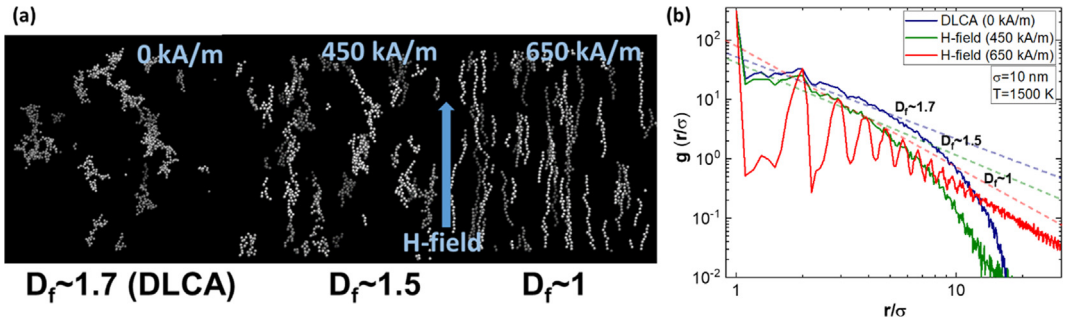

Fig. 2. (a) Visual representation of DLCA aggregates (in absence of H-field), low dimensional aggregates and linear chain-like aggregates in presence of H-field ~ 450 kA/m and 650 kA/m respectively, (b) Pair-correlation function of DLCA aggregates with D_f ~ *1.7* (in absence of H-field), low dimensional aggregates with D_f ~ *1.5* (H-field ~ 450 kA/m) and linear aggregates with D_f ~ *1* (H-field ~ 650 kA/m) having peak and valley features, for ferromagnetic primary particles of size 10 nm at 1500 K.

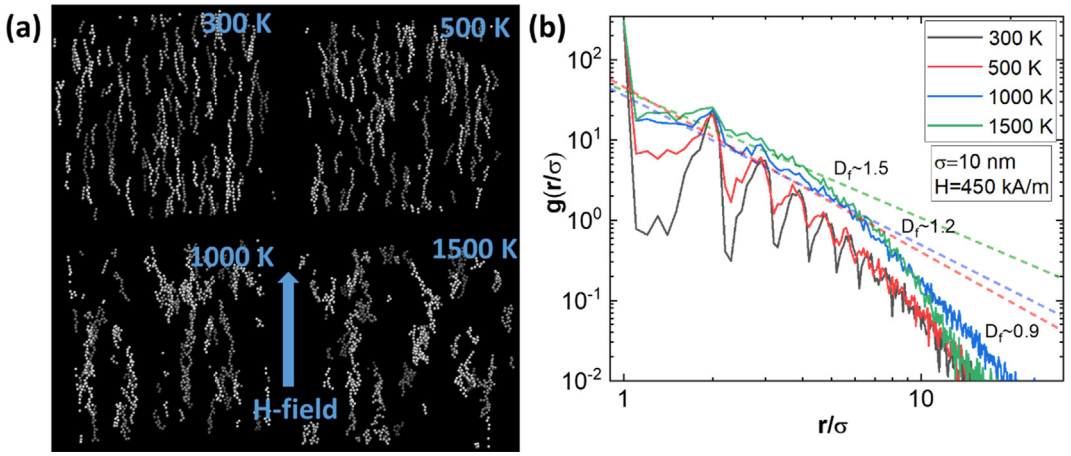

Fig. 3. Visual representation (a) and pair-correlation function (b) of aggregates formed by ferromagnetic primary particles of size 10 nm in presence of H-field (450 kA/m) at different temperatures (300–1500 K). The linearity in the visual representation and the peak-valley features in the pair-correlation function are only retained till 500 K.

dipole interactions are required to overpower the random Brownian fluctuations. Since, the magnetic interactions depend on σ and H, whereas the Brownian fluctuations are dependent on σ and T, it is essential to study the manner in which the combination of these variables affect the overall aggregation process, analysis of which is done in the subsequent sections.

3.2. Aggregate shape transition with temperature for a constant H-field

Fig. 3(a) shows the visual representation of aggregates formed by primary particles of size $\sigma = 10nm$, in an applied H-field strength of *450 kA/m*, at different temperatures 300–1500 K. From Fig. 3(a) it is evident that the aligned and linear aggregate growth is most prevalent at lower temperatures (300–500 K), where Brownian dynamics are slower. Fig. 3(b) shows that the pair-correlation function loses the peak and valley features above 500 K, consistent with the structure images. However, the aggregates obtained at 1000 K (D_f 1.2) and 1500 K (D_f 1.5) are low dimensional compared to DLCA aggregates (D_f 1.7) obtained in the absence of field.

Even though the fractal dimension is changed at higher temperature, according to Fig. 3(a) the alignment with the H-field is still retained. This is because the growth is initiated with occupancy of the nearest neighboring sites, which involves strong dipolar interactions responsible for growth in the direction of H-field. However, the r^{-3}, decaying interaction strength, might not be enough to influence the collisions at further neighboring sites.

3.3. Threshold field intensity for directed linear assembly

As the assembly into linear aggregates is dependent on primary particle size and temperature, we evaluate the threshold H-field strength required for successful assembly. Fig. 4 shows the threshold H-field strength required for successful assembly for different primary particle sizes at different temperatures. The field strengths at which more than 4 peaks at integral multiples of the monomer diameter, appear in the pair-correlation functions, are considered to be the threshold. The required threshold decreases with increase in particle size. However, temperature only affects the lower particle sizes which follow ballistic trajectory. Hence, temperature only affects the aggregation in the ballistic regime, while size affects both ballistic and diffusive regimes. In the ballistic limit of the free-molecular regime, a strong external force is required to influence the trajectories of particles having very high persistence lengths. The directional repulsive interactions at the lateral edges ($\theta > 0 or < \pi$) of the aggregates are most important for the formation of linear chains. In a simple 1-D model of one monomer approaching another monomer, with mean velocity $\sqrt{\frac{k_B T}{m_p}}$ along a direction perpendicular to the applied magnetic field ($\theta = \frac{\pi}{2}$), the condition $\frac{F_H}{m_p} \geq \sqrt{\frac{k_B T}{m_p}} \frac{\xi}{m_p} \frac{\sigma}{l_0}$ should hold, for the repulsive force of one monomer to negatively accelerate the approaching monomer to a stationary state, at a minimum separation of σ (supplemental, S.4). The field equivalent to generate the minimum repulsive force to satisfy the above condition, is the threshold field required for the linear assembly. Deriving F_H from 1-D version of Eq. (7), one can arrive at the equation $\frac{H_{th}\sigma^{1.5}}{T^{0.5}} = C$, where H_{th} is the threshold H-field, and C is a constant (supplemental, S.4). This approximately explains the trend observed in Fig. 4 as well as the negative slope of ~−1.7–1.9 in the logarithmic version of Fig. 4 (supplemental, Fig. S1)

For a comparison, a case of the threshold electric field (E-field) required for assembly of pre-aligned electric dipoles in ferroelectric particles at 1000 K, obtained by doing simulations in the same manner (details in supplemental, Section S.5), has also been presented. It is evident that the threshold E-fields required for

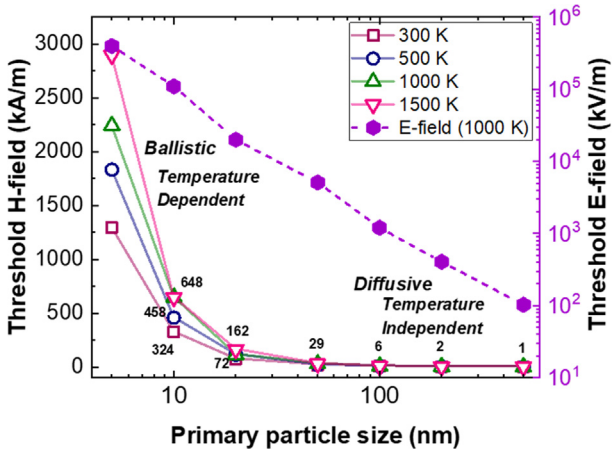

Fig. 4. Threshold H-field required for linear assembly ($D_f \sim 1$) for different primary particle sizes (5–500 nm) and at different temperatures (300–500 K). Threshold E-field for the same assembly for same primary particle sizes at 1000 K has been shown for comparison. Ballistic trajectory contributes to the temperature dependence.

successful assembly of primary particle sizes <100 nm are beyond practicality, as the required fields exceed the breakdown field strength of air and most inert gases (~3000 kV/m) [47].

3.4. Coagulation time scales and kernel homogeneity

To understand growth kinetics the simulation was initiated with a number concentration of ~ $4 \times 10^{21}/m^3$ monomers. The monomer concentration was tracked and the simulation time-steps converted to real time by the scaling discussed in Section 2.2. Fig. 5(a) shows the depression in monomer ($\sigma = 10nm$) concentration with increasing time for different H-field strengths at 1500 K. The strong attractive forces due to the H-field, increases the coagulation rate, and this effect is observed even for field strengths below the threshold field strength required for assembly. The inset of Fig. 5(a) shows the decreasing half-life ($t_{1/2}$) of the monomer concentration with increasing H-field strengths, resulting from the enhanced coagulation rates.

The coagulation of fractal aggregates follows $\frac{1}{n_1(t)} - \frac{1}{n_0} = Kt^z$, where $z = \frac{1}{1-\lambda}$, λ being the homogeneity of the coagulation kernel [23]. Fig. 5(b) shows the log-log plot of this equation at various applied field strengths, where z and λ, have been estimated from the slope of the linear trend upto 10^{-7} s. z decreases whereas λ increases, with an increase in H-field strength.

3.5. Magnetization vs coagulation rates of linear assembly of ferromagnetic and superparamagnetic particles

The simulation starts with the assumption that all the primary particles are pre-magnetized with a net magnetic anisotropy in the form of dipoles, either in parallel ($\theta = 0$) or anti-parallel ($\theta = \pi$) to the applied H-field, typically known as the discrete-orientation approximation [48]. For static, ferromagnetic particles, at temperatures below the Curie point, this approximation holds true when a sufficiently high H-field is applied such that the thermal fluctuation energy (k_BT) is negligible compared to the demagnetization potential energy ($2pHcos\theta$) [49]. The demagnetization potential associated with the required threshold fields (Fig. 4) at different temperatures, are orders of magnitude higher than the respective thermal energy (Table S1). In the case of an oscillating H-field, this approximation implies that the oscillation frequency of the dipoles will be equal to that of the field. However, for ferromagnetic particles undergoing Brownian dynamics at temperatures below the Curie point, the discrete-orientation approximation will hold true only if the period of oscillation of the dipoles (i.e. H-field), is faster than coagulation.

At temperatures above the Curie point or at weaker H-fields, the demagnetization potential will be comparable or less than the thermal energy. In this case, the approximation will still apply for sub-50 nm ferromagnetic particles which are nominally single domain and hence exhibit superparamagnetism [50], only if the demagnetization time-scales are small compared to both H-field period [48] and coagulation time-scales. The net magnetic anisotropy or dipole needs to relax to a de-aligned state (zero-energy) from an aligned state (lowest energy), faster than the rate of change of the H-field, in order to keep the dipole always in an equilibrium alignment with the field. For superparamagnetic particles undergoing Brownian dynamics, the fast relaxation can be caused by either intra-particle domain relaxation by electronic spin exchange which can be estimated from the the Néel relaxation time (τ_s) [51,52] or domain relaxation by external Brownian rotation. The Brownian rotational time-scales (τ_B) have been estimated by considering ballistic and diffusive rotations in free-molecular and transition regimes (supplemental, S6). The net domain relaxation time scale is the harmonic mean of the Néel relaxation and the Brownian rotational relaxation time-scales, as given by $\tau_{net} = \frac{\tau_s \tau_B}{\tau_s + \tau_B}$ [53]. The values estimated for each of these time-scales have been presented in Tables S3–S6.

To estimate the theoretical coagulation time-scales, the Smoluchowski's coagulation kernel has been corrected for both free molecular and transition regimes as described in Section 2.3, and the theoretical $t_{1/2}$has been estimated using the corrected kernel. Fig. 6(a) shows the enhancement factors, and $t_{1/2}$values estimated from the corrected theoretical kernel, at different applied field strengths, for 10 nm particles at 300 K (transition) and 1500 K (free molecular). The $t_{1/2}$values estimated from theory at 1500 K, approximately has the same order of magnitude, compared to the $t_{1/2}$values estimated from the simulation at 1500 K (Inset, 5 (a)). The approximate match between the theoretical and computational $t_{1/2}$, and the estimation of interaction dependent coagulation rates in both regimes, enables us to use the theoretical equation to estimate the coagulation time-scales of an ensemble of monomers, with practical aerosol phase number concentrations of 10^{14}–$10^{18}/m^3$ [8].

Fig. 6(b) shows the comparison between time-scales of superparamagnetic domain relaxation, ferromagnetic magnetization

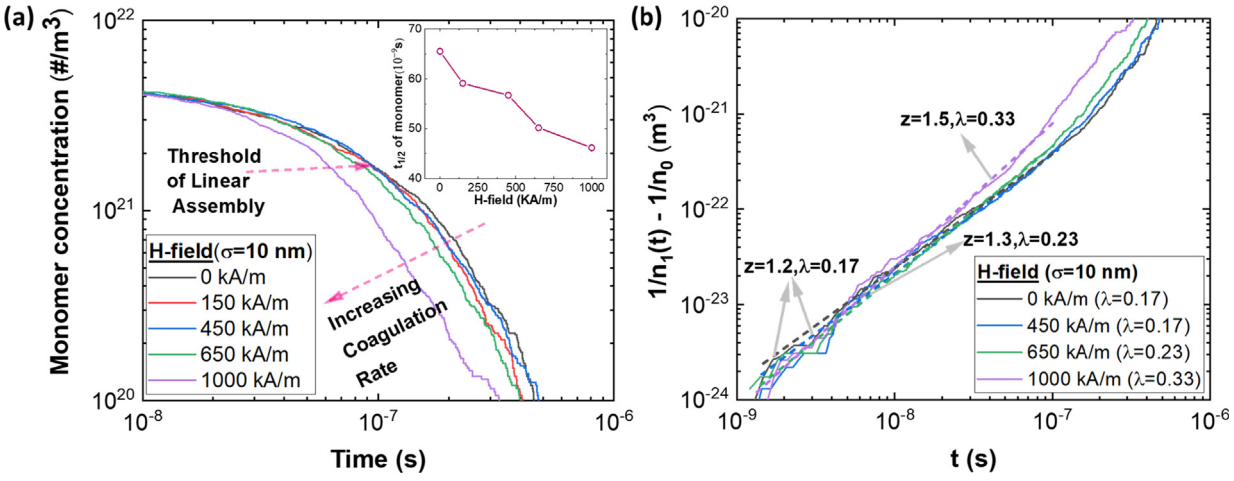

Fig. 5. (a) Monomer (10 nm) concentration with time from the simulation at 1500 K. Rate of decrease in monomer concentration increases with H-field strength. Inset shows the half-lives ($t_{1/2}$) of the monomers decreases with increase in H-field strength. (b) Estimation of the homogeneity of the coagulation kernel (λ), which increases with increase in for the applied H-field strength.

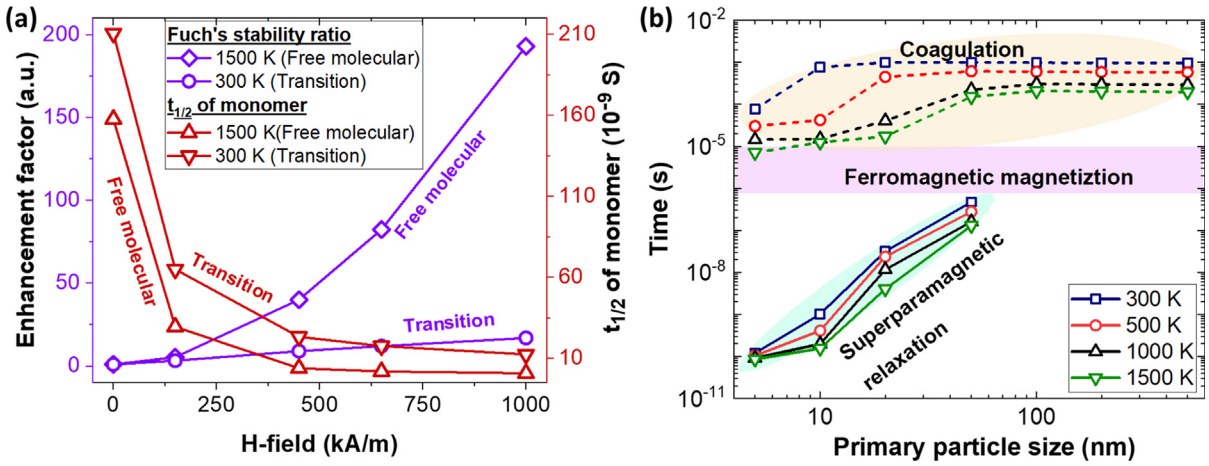

Fig. 6. (a) Enhancement factor and comparison between theoretically estimated monomer half-lives ($t_{1/2}$) of free-molecular (1500 K) and transition regime (300 K). (b) Comparison between time-scales of superparamagnetic domain relaxation, ferromagnetic magnetization (H-field oscillation) and coagulation, for primary particle number concentration ($10^{18}/m^3$), for different primary particle sizes (5–500 nm) and different temperatures (300–1500 K).

Table 1
Design parameters required for the linear assembly of Fe, Co and Ni.

Material	Curie point [54](K)	H-field Frequency (Hz) /strength (kA/m)	Ferromagneticassembly		Superparamagnetic assembly	
			Size (nm)	T (K)	Size (nm)	T (K)
Fe	1043	10^6–10^5/10–10^3	10–500	300–1043	10–50	>1043
Co	1400	10^6–10^5/10–10^3	10–500	300–1400	10–50	>1400
Ni	627	10^6–10^5/10–10^3	10–500	300–627	10–50	>627

(H-field oscillation) and coagulation for different primary particle sizes, at different temperatures. For this comparison, the coagulation time-scales have been estimated theoretically for a practical aerosol number concentration of $10^{18}/m^3$. As commonly applied H-fields have oscillation time-period (10^5–10^6 Hz) smaller than the coagulation time-scales, the discrete-orientation approximation will be consistent for all particle sizes below Curie temperature, at these frequencies. For sub-50 nm primary particle sizes, time-scales of superparamagnetic relaxation are shorter by orders of magnitude compared to the standard time period of oscillation of the H-field. This implies that sub-50 nm particles will always be in an equilibrium alignment with the field, and will follow the oscillation of the field, at any field strength and temperature. Also, since both the relaxation time and the time period of oscillation is shorter by orders of magnitude compared to the coagulation time-scales, the discrete-orientation approximation will be consistent for the super-paramagnetic particles at all sizes and temperatures.

As discussed in Section 3.3, the threshold H-fields required for linear assembly of primary particle sizes $\geq 10nm$, are practically achievable at temperatures between 300 and 1500 K. Hence, if the applied field is higher than the threshold field, all ferromagnetic particles can be linearly assembled at temperatures below their respective Curie points. Above, the Curie point, only superparamagnetic particles in the size range 10–50 nm can be assembled. Table 1 shows the summary of the design parameters applicable to linearly assemble Fe, Ni and Co, which show both ferromagnetism and superparamagnetism.

Alloys of Fe, Co and Ni with *para*-magnetic metals such as Al, Cu, Pd etc. also shows ferromagnetic and super-paramagnetic behaviour [55–58]. Hence, *para*-magnetic metal particles like Al, Cu, Pd etc. when alloyed with Fe, Co and Ni can also be linearly assembled with an external H-field. Pulsed laser ablation, flame synthesis, chemical vapor deposition [1], inert gas condensation [59] are some of the most common aerosol routes to synthesize both monometallic and alloyed metal particles. Using the parameters represented in Table 1, one can design a magnetic coil in the vicinity of the substrates or chambers used in these synthesis procedures, to apply an oscillating magnetic field of desired strength, to direct the assembly of magnetic, metal and alloyed-metal nanoparticles.

4. Conclusion

Cluster-cluster aggregation simulations, typically used to understand aggregation and assembly processes in colloidal systems [15,17,34,46,60–63], have been employed through a hybrid Monte Carlo method, to demonstrate that externally applied magnetic fields can be used to direct the assembly of aerosol nanoparticles of ferromagnetic materials (Fe, Co, Ni, etc.), in both free-molecular and transition regimes. Application of an external field (electric or magnetic) induces a net magnetic dipole moment, within ferromagnetic (or ferroelectric) particles, which interact with each other through directional attraction and repulsion, ultimately leading to the growth of linear chain-like aggregates, as shown by several studies in the continuum regime [18]. However, in aerosol systems where the free-molecular and transition regimes are also simulated, a significant structure transition from $D_f \sim 1.8$ have not been found earlier [23,25,37,45]. The simulations performed in this study indicate that magnetic dipolar interactions induced by external H-field can be used to cause such structure transition from the universal $D_f \sim 1.8$ to $D_f \sim 1$, which have been also found in our experimental study [22]. By performing simulations for different particle sizes 5–500 nm and different temperature 300–1500 K, we find that the threshold H-field strength required for the linear assembly is both particle size and

temperature dependent in the size range 5–50 nm. The threshold H-fields required for 10–100 nm particles are practically achievable, whereas the corresponding E-field threshold will be beyond breakdown strength of air. Given that the applied H-field is higher than the threshold, through analysis of the coagulation and magnetization time-scales, we show that primary particle sizes < 50 nm will be magnetized and hence linearly assembled, at all temperatures. The results published in this work will be useful to material designers working on scalable fabrication of metal and alloyed metal nanocomposites in gas phase, with tunable micro-structural features, enabling possibilities for density, mechanical, and optical property modulation in the final materials of interest.

CRediT authorship contribution statement

Prithwish Biswas: Methodology, Formal analysis, Writing-original draft. **Pankaj Ghildiyal:** Methodology, Visualization, Writing-review & editing. **George W. Mulholland** Methodology, Validation, Writing-review & editing. **Michael R. Zachariah:** Conceptualization, Project administration, Methodology, Writing-original draft, review & editing.

Declaration of Competing Interest

The authors declare that they have no known competing financial interests or personal relationships that could have appeared to influence the work reported in this paper.

Acknowledgements

We gratefully acknowledge support from an ONR-MURI grant. We also thank the TCB group at UIUC for the VMD visualization package used for creating the particle visual representations.

Appendix A. Supplementary data

Supplementary data to this article can be found online at https://doi.org/10.1016/j.jcis.2021.02.050.

References

[1] M.T. Swihart, Vapor-phase synthesis of nanoparticles, Curr. Opin. Colloid Interface Sci. (2003), https://doi.org/10.1016/S1359-0294(03)00007-4.
[2] M. Ullmann, S.K. Friedlander, A. Schmidt-Ott, Nanoparticle formation by laser ablation, J. Nanoparticle Res. (2002), https://doi.org/10.1023/A:1022840924336.
[3] A.D. Franklin, M. Luisier, S.J. Han, G. Tulevski, C.M. Breslin, L. Gignac, M.S. Lundstrom, W. Haensch, Sub-10 nm carbon nanotube transistor, Nano Lett. (2012), https://doi.org/10.1021/nl203701g.
[4] G.A. Kelesidis, E. Goudeli, S.E. Pratsinis, Flame synthesis of functional nanostructured materials and devices: Surface growth and aggregation, Proc. Combust. Inst. (2017), https://doi.org/10.1016/j.proci.2016.08.078.
[5] L. Zhong, T. Kwok, L. Mangolini, Spray pyrolysis of yolk-shell particles and their use for anodes in lithium-ion batteries, Electrochem. Commun. (2015), https://doi.org/10.1016/j.elecom.2015.02.004.
[6] Y. Yang, M. Romano, G. Feng, X. Wang, T. Wu, S. Holdren, M.R. Zachariah, Growth of Sub-5 nm Metal Nanoclusters in Polymer Melt Aerosol Droplets, Langmuir 34 (2018) 585–594, https://doi.org/10.1021/acs.langmuir.7b02900.
[7] Y. Yang, P. Ghildiyal, M.R. Zachariah, Thermal Shock Synthesis of Metal Nanoclusters within On-the-Fly Graphene Particles, Langmuir (2019), https://doi.org/10.1021/acs.langmuir.8b03532.
[8] S. Friedlander, Smoke, dust and haze. Fundamentals of aerosol behaviour, 1977. https://doi.org/10.1016/0004-6981(79)90129-x.
[9] E.D. Goddard, Surfactants and interfacial phenomena, Colloids Surf. (1989), https://doi.org/10.1016/0166-6622(89)80030-7.
[10] H.C. Hamaker, The London-van der Waals attraction between spherical particles, Physica (1937), https://doi.org/10.1016/S0031-8914(37)80203-7.
[11] R.D. Mountain, G.W. Mulholland, Light Scattering from Simulated Smoke Agglomerates, Langmuir 4 (1988) 1321–1326, https://doi.org/10.1021/la00084a021.
[12] R. Gopalakrishnan, M.J. Meredith, C. Larriba-Andaluz, C.J. Hogan, Brownian dynamics determination of the bipolar steady state charge distribution on spheres and non-spheres in the transition regime, J. Aerosol Sci. (2013), https://doi.org/10.1016/j.jaerosci.2013.04.007.
[13] R. Gopalakrishnan, T. Thajudeen, H. Ouyang, C.J. Hogan, The unipolar diffusion charging of arbitrary shaped aerosol particles, J. Aerosol Sci. (2013), https://doi.org/10.1016/j.jaerosci.2013.06.002.
[14] R. Gopalakrishnan, C.J. Hogan, Coulomb-influenced collisions in aerosols and dusty plasmas, Phys. Rev. E - Stat. Nonlinear, Soft Matter Phys. (2012), https://doi.org/10.1103/PhysRevE.85.026410.
[15] P.M. Mors, R. Botet, R. Jullien, Cluster-cluster aggregation with dipolar interactions, J. Phys. A: Math. Gen. 20 (1987) L975–L980, https://doi.org/10.1088/0305-4470/20/15/008.
[16] J.G. Ku, X.Y. Liu, H.H. Chen, R.D. Deng, Q.X. Yan, Interaction between two magnetic dipoles in a uniform magnetic field, AIP Adv. 6 (2016), https://doi.org/10.1063/1.4941750.
[17] Z.J. Tan, X.W. Zou, W.B. Zhang, Z.Z. Jin, Structure transition in cluster-cluster aggregation under external fields, Phys. Rev. E - Stat. Physics, Plasmas, Fluids, Relat. Interdiscip. Top. (2000), https://doi.org/10.1103/PhysRevE.62.734.
[18] G. Helgesen, A.T. Skjeltorp, P.M. Mors, R. Botet, R. Jullien, Aggregation of magnetic microspheres: Experiments and simulations, Phys. Rev. Lett. 61 (1988) 1736–1739, https://doi.org/10.1103/PhysRevLett.61.1736.
[19] S.G. Johnson, P.R. Villeneuve, S. Fan, J.D. Joannopoulos, Linear waveguides in photonic-crystal slabs, Phys. Rev. B - Condens. Matter Mater. Phys. (2000), https://doi.org/10.1103/PhysRevB.62.8212.
[20] E.R. Cintra, F.S. Ferreira, J.L. Santos Junior, J.C. Campello, L.M. Socolovsky, E.M. Lima, A.F. Bakuzis, Nanoparticle agglomerates in magnetoliposomes, Nanotechnology (2009), https://doi.org/10.1088/0957-4484/20/4/045103.
[21] Z. Li, M. Wang, X. Zhang, D. Wang, W. Xu, Y. Yin, Magnetic Assembly of Nanocubes for Orientation-Dependent Photonic Responses, Nano Lett. (2019), https://doi.org/10.1021/acs.nanolett.9b02984.
[22] P. Ghildiyal, P. Biswas, H. Steven, G.W. Mulholland, Y. Yang, R. Abbaschian, M. R. Zachariah, Magnetic-Field Directed Vapor-Phase Assembly of Low Fractal Dimension Metal Nanostructures: Experiment and Theory (Under Review), J. Phys. Chem. Lett. (2021).
[23] W.R. Heinson, F. Pierce, C.M. Sorensen, A. Chakrabarti, Crossover from ballistic to epstein diffusion in the free-molecular regime, Aerosol Sci. Technol. 48 (2014) 738–746, https://doi.org/10.1080/02786826.2014.922677.
[24] T. Thajudeen, S. Deshmukh, C.J. Hogan, Langevin simulation of aggregate formation in the transition regime, Aerosol Sci. Technol. (2015), https://doi.org/10.1080/02786826.2015.1008971.
[25] R. Gopalakrishnan, C.J. Hogan, Determination of the transition regime collision kernel from mean first passage times, Aerosol Sci. Technol. (2011), https://doi.org/10.1080/02786826.2011.601775.
[26] R. Gopalakrishnan, T. Thajudeen, C.J. Hogan, Collision limited reaction rates for arbitrarily shaped particles across the entire diffusive Knudsen number range, J. Chem. Phys. (2011), https://doi.org/10.1063/1.3617251.
[27] B. Hunt, T. Thajudeen, C.J. Hogan, The single-fiber collision rate and filtration efficiency for nanoparticles i: The first-passage time calculation approach, Aerosol Sci. Technol. (2014), https://doi.org/10.1080/02786826.2014.938798.
[28] T. Thajudeen, B. Hunt, C.J. Hogan, The single-fiber collision rate and filtration efficiency for nanoparticles ii: Extension to arbitrary-shaped particles, Aerosol Sci. Technol. (2014), https://doi.org/10.1080/02786826.2014.938799.
[29] G.J. Lindquist, D.Y.H. Pui, C.J. Hogan, Porous particulate film deposition in the transition regime, J. Aerosol Sci. (2014), https://doi.org/10.1016/j.jaerosci.2014.03.007.
[30] H.S. Chahl, R. Gopalakrishnan, High potential, near free molecular regime Coulombic collisions in aerosols and dusty plasmas, Aerosol Sci. Technol. (2019), https://doi.org/10.1080/02786826.2019.1614522.
[31] H. Ouyang, R. Gopalakrishnan, C.J. Hogan, Nanoparticle collisions in the gas phase in the presence of singular contact potentials, J. Chem. Phys. (2012), https://doi.org/10.1063/1.4742064.
[32] L. Li, R. Gopalakrishnan, An experimentally validated model of diffusion charging of arbitrary shaped aerosol particles, J. Aerosol Sci. (2021), https://doi.org/10.1016/j.jaerosci.2020.105678.
[33] L. Li, H.S. Chahl, R. Gopalakrishnan, Comparison of the predictions of Langevin Dynamics-based diffusion charging collision kernel models with canonical experiments, J. Aerosol Sci. (2020), https://doi.org/10.1016/j.jaerosci.2019.105481.
[34] S. Jungblut, J.O. Joswig, A. Eychmüller, Diffusion-Limited Cluster Aggregation: Impact of Rotational Diffusion, J. Phys. Chem. C 123 (2019) 950–954, https://doi.org/10.1021/acs.jpcc.8b10805.
[35] X. Bian, C. Kim, G.E. Karniadakis, 111 years of Brownian motion, Soft Matter 12 (2016) 6331–6346, https://doi.org/10.1039/c6sm01153e.
[36] G.W. Mulholland, R.D. Mountain, R.J. Samson, M.H. Ernst, Cluster Size Distribution for Free Molecular Agglomeration, Energy Fuels 2 (1988) 481–486, https://doi.org/10.1021/ef00010a014.
[37] C.M. Sorensen, The mobility of fractal aggregates: A review, Aerosol Sci. Technol. (2011), https://doi.org/10.1080/02786826.2011.560909.
[38] T.D. Yensen, What is the magnetic permeability of iron?, J. Franklin Inst. (1928), https://doi.org/10.1016/S0016-0032(28)90558-X.
[39] G.R. Wait, Magnetic permeability of iron and magnetite in high frequency alternating fields, Phys. Rev. (1927), https://doi.org/10.1103/PhysRev.29.566.

[40] P. Koskela, M. Teirikangas, A. Alastalo, J. Forsman, J. Juuti, U. Tapper, A. Auvinen, H. Seppä, H. Jantunen, J. Jokiniemi, Synthesis of cobalt nanoparticles to enhance magnetic permeability of metal-polymer composites, Adv. Powder Technol. (2011), https://doi.org/10.1016/j.apt.2010.09.010.
[41] D. Frenkel, B. Smit, Monte Carlo Simulations in Various Ensembles, Underst. Mol. Simul. (2002), https://doi.org/10.1016/b978-012267351-1/50007-9.
[42] M. Moinuddin, P. Biswas, M. Tripathy, The effect of surface roughness on the phase behavior of colloidal particles, J. Chem. Phys. 152 (2020), https://doi.org/10.1063/1.5136080.
[43] R.D. Mountain, G.W. Mulholland, H. Baum, Simulation of aerosol agglomeration in the free molecular and continuum flow regimes, J. Colloid Interface Sci. 114 (1986) 67–81, https://doi.org/10.1016/0021-9797(86)90241-9.
[44] M. Mellema, J.H.J. Van Opheusden, T. Van Vliet, Relating colloidal particle interactions to gel structure using Brownian dynamics simulations and the Fuchs stability ratio, J. Chem. Phys. (1999), https://doi.org/10.1063/1.479956.
[45] C.M. Sorensen, Light scattering by fractal aggregates: A review, Aerosol Sci. Technol. (2001), https://doi.org/10.1080/02786820117868.
[46] M. Lattuada, H. Wu, M. Morbidelli, A simple model for the structure of fractal aggregates, J. Colloid Interface Sci. 268 (2003) 106–120, https://doi.org/10.1016/j.jcis.2003.07.027.
[47] M. Abdel-Salam, H. Anis, A. El-Morshedy, R. Radwan, M. Abdel-Salam, Electrical Breakdown of Gases, High-Voltage Eng. (2018), https://doi.org/10.1201/9781482290035-4.
[48] W.F. Brown, Thermal fluctuations of a single-domain particle, Phys. Rev. (1963), https://doi.org/10.1103/PhysRev.130.1677.
[49] D.C. Jiles, D.L. Atherton, Theory of ferromagnetic hysteresis, J. Magn. Magn. Mater. (1986), https://doi.org/10.1016/0304-8853(86)90066-1.
[50] V. Marghussian, Magnetic Properties of Nano-Glass Ceramics, in, Nano-Glass Ceram. (2015), https://doi.org/10.1016/b978-0-323-35386-1.00004-9.
[51] S. Ota, Y. Takemura, Characterization of Néel and Brownian Relaxations Isolated from Complex Dynamics Influenced by Dipole Interactions in Magnetic Nanoparticles, J. Phys. Chem. C 123 (2019) 28859–28866, https://doi.org/10.1021/acs.jpcc.9b06790.
[52] J. Dieckhoff, D. Eberbeck, M. Schilling, F. Ludwig, Magnetic-field dependence of Brownian and Néel relaxation times, J. Appl. Phys. 119 (2016), https://doi.org/10.1063/1.4940724.
[53] R.J. Deissler, Y. Wu, M.A. Martens, Dependence of Brownian and Néel relaxation times on magnetic field strength, Med. Phys. 41 (2014), https://doi.org/10.1118/1.4837216.
[54] C. Kittel, Introduction to Solid State Physics, eighth ed., Wiley Sons, New York, NY, 2004.
[55] R. Kulkarni, B.S. Murty, V. Srinivas, Study of microstructure and magnetic properties of AlNiCo(CuFe) high entropy alloy, J. Alloy. Compd. (2018), https://doi.org/10.1016/j.jallcom.2018.02.275.
[56] S. Vrtnik, S. Guo, S. Sheikh, A. Jelen, P. Koželj, J. Luzar, A. Kocjan, Z. Jagličić, A. Meden, H. Guim, H.J. Kim, J. Dolinšek, Magnetism of CoCrFeNiZrx eutectic high-entropy alloys, Intermetallics (2018), https://doi.org/10.1016/j.intermet.2017.11.017.
[57] R. Nazir, M. Mazhar, M.J. Akhtar, M. Raza Shah, N.A. Khan, M. Nadeem, M. Siddique, M. Mehmood, N.M. Butt, Superparamagnetic bimetallic iron-palladium nanoalloy: Synthesis and characterization, Nanotechnology (2008), https://doi.org/10.1088/0957-4484/19/18/185608.
[58] M. Vondrova, T. Klimczuk, V.L. Miller, B.W. Kirby, N. Yao, R.J. Cava, A.B. Bocarsly, Supported superparamagnetic Pd/Co alloy nanoparticles prepared from a silica/cyanogel Co-gel, Chem. Mater. (2005), https://doi.org/10.1021/cm051244r.
[59] A. Maisels, F.E. Kruis, H. Fissan, B. Rellinghaus, H. Zähres, Synthesis of tailored composite nanoparticles in the gas phase, Appl. Phys. Lett. (2000), https://doi.org/10.1063/1.1335843.
[60] S. Lazzari, L. Nicoud, B. Jaquet, M. Lattuada, M. Morbidelli, Fractal-like structures in colloid science, Adv. Colloid Interface Sci. 235 (2016) 1–13, https://doi.org/10.1016/j.cis.2016.05.002.
[61] S. Jungblut, J.O. Joswig, A. Eychmüller, Diffusion- and reaction-limited cluster aggregation revisited, PCCP 21 (2019) 5723–5729, https://doi.org/10.1039/c9cp00549h.
[62] F. Kogler, O.D. Velev, C.K. Hall, S.H.L. Klapp, Generic model for tunable colloidal aggregation in multidirectional fields, Soft Matter 11 (2015) 7356–7366, https://doi.org/10.1039/c5sm01103e.
[63] S. Kim, K.S. Lee, M.R. Zachariah, D. Lee, Three-dimensional off-lattice Monte Carlo simulations on a direct relation between experimental process parameters and fractal dimension of colloidal aggregates, J. Colloid Interface Sci. 344 (2010) 353–361, https://doi.org/10.1016/j.jcis.2010.01.008.